Microstructural evolution during long time aging of 15–5PH stainless steel

Laurent Couturier, Frédéric de Geuser, Alexis Deschamps

To cite this version:

Laurent Couturier, Frédéric de Geuser, Alexis Deschamps. Microstructural evolution during long time aging of 15–5PH stainless steel. Materialia, 2020, 9, pp.100634. ⟨10.1016/j.mtla.2020.100634⟩. ⟨hal-02507477⟩

Microstructural evolutions during long time aging of 15-5PH stainless steel

Laurent Couturier[1,2], Frédéric De Geuser[1], Alexis Deschamps[1]

[1] Univ. Grenoble Alpes, CNRS, Grenoble INP, SIMAP, 38000 Grenoble, France

[2] Institut des Matériaux Jean Rouxel (IMN), Université de Nantes, CNRS, 2 rue de la Houssinière, BP 32229, 44322 Nantes Cedex 3, France

Abstract

When subjected to long-term aging at intermediate temperatures, the 15-5PH precipitation hardening martensitic stainless steel is subject to a complex evolution of its microstructure that impacts its service mechanical properties. This evolution includes possible evolution of minor austenite phase, of the copper-rich precipitates, as well as unmixing of the chromium solid solution and formation of silicon-rich precipitates. In this work, a systematic quantification of all these evolutions as a function of aging temperature and time is obtained by combining advanced characterization tools, notably phase and orientation mapping in the transmission electron microscope, atom probe tomography, and small angle X-ray and neutron scattering. Results show a remarkable stability of austenite and Cu precipitation, and evidence the kinetics of Cr unmixing and Si-rich phase formation. We proposed a phenomenological model for the Cr composition fluctuations' amplitude and characteristic length increase with aging and put it in relation to hardness' evolution.

Corresponding author: Laurent Couturier, laurent.couturier@univ-nantes.fr

1. Introduction

The 15-5PH is a high strength martensitic stainless steel hardened thanks to copper precipitation. A possible application for this kind of stainless steel is as constitutive material of structural parts of airplane pylons. During use, due to the proximity of the pylon to the engine, the 15-5PH undergoes thermal aging at relatively low temperatures, around 300°C, leading to a significant change of the mechanical behavior of the alloy [1–6] that may lead to a decrease in toughness. This change in mechanical properties of the material is caused by evolutions of its complex initial microstructure, which we have presented in details in a former work [7]. The two main microstructural changes during such stainless steels' aging are the precipitation of a Ni, Mn and Si-rich phase and the Fe-Cr matrix unmixing, both at the nanometer scale [8–12].

Precipitation of Ni, Mn and Si-rich phase in stainless steels, usually of the duplex kind used for nuclear applications, has been extensively studied in the last years [13–23]. The precipitated phase is usually designated as G-phase, which has been very well characterized since its first observation by Beattie et al. in 1956, both in terms of crystallographic structure – face centered cubic with a lattice parameter around four times the ferrite's lattice parameter – and composition – that may be complex but is usually depicted as $Mn_6Si_7Ni_{16}$ [21,22,24–32]. The impact of this precipitation on mechanical properties is still under study, some authors claiming it has no or negligible influence [5,28,33] and others claiming a significant impact [34,35]. Nonetheless, in stainless steels where G-phase precipitation occurs as well as Fe-Cr unmixing, most authors consider that the two phenomena are coupled. Mateo et al. even proposed a G-phase formation mechanism driven by the partitioning of elements during the Fe-Cr unmixing evolution [24]. Other authors also reported heterogeneous precipitation on dislocations or other precipitated phases leading to a bi-modal precipitates distribution [14,18,22,23].

The Fe-Cr unmixing has also been the focus of a large number of studies since the theories of Cahn et al. [36–38] until very recent reports [11,12,15,20,34,39–50] with both an experimental and/or a numerical approach. Cahn and Hilliard were the firsts to propose a model for the early stages of spinodal decomposition in solids [36]. Then Langer, Bar-on and Miller (LBM theory), proposed a description of the evolution of the structure factor of the spinodal decomposition using Monte Carlo (MC) kinetics [51]. Further works also focused on the prediction of Fe-Cr unmixing using MC kinetics leading to a description of the unmixing's structure factor and/or characteristic size evolution with time. The evolution is always modeled using a power-law of aging time but with various time exponents [52–64].

These predictions may be confronted with experimental studies. In particular, atom probe tomography (APT) has been extensively used for the Fe-Cr unmixing's characterization [39,52,63–68] since this technique is the only one being able to characterize directly local compositional changes at the atomic scale, which is the scale of the Fe-Cr unmixing in its early stages. These experimental works have been supported with fewer articles using small-angle scattering techniques (essentially with neutrons - SANS) [69–72]. However, even with these advanced characterization techniques, describing the Fe-Cr unmixing is rather complex. Blavette et al. proposed to use the V-parameter determined with APT, linked mainly (but indirectly) to the composition fluctuations' amplitude, to describe the advancement of the unmixing reaction [73]. This parameter was found to be proportional to the ferrite's hardness increment in some duplex stainless steels [65,66]. More recently, the Chalmers group proposed to use the Cr RDF (Radial Distribution Function), still determined with APT, to estimate the characteristic size and amplitude of the Cr composition fluctuations, the Cr RDF being directly linked to the Cr autocorrelation function [74]. They showed recently thanks to this use of RDF the proportionality between Cr composition fluctuations' amplitude and hardness increment of the ferrite of the 2507 super duplex stainless steel [11]. Most of these works were made considering the ferrite of duplex stainless steels, or even Fe-Cr binary alloys for the study of Fe-Cr unmixing, which contain higher levels of Cr than the material under study in this work and also different alloying elements' contents, especially Ni, whose effect on the Fe-Cr unmixing kinetics has been shown by different authors [46,47,75–77]. This quite low Cr content makes it possible that the unmixing reaction would follow the nucleation and growth mechanism rather than the spinodal decomposition one – at least it would be the case at the considered temperatures if the material under study has been a binary alloy with similar Cr content. Although this paper only considering the very early stage of unmixing, the evolution of the Cr composition fluctuations would be very similar in both mechanisms, except for their time exponent – presented in the above paragraph. Thus we will not in the following refer to one or the other mechanism and only describe the Cr composition fluctuations' evolution with aging time. The presence of the Cu-rich precipitation that ensures the material high strength may also interfere with these microstructural evolutions.

The present work is an experimental approach based on the convergence of different characterization techniques, listed in section 2, so that all microstructural changes during long term aging, up to 15000h, in a large temperature interval from 290°C to 420°C may be observed and quantitatively described. It completes our previous work, which described in more details the initial microstructure – before aging – of the material under study [7] and presented a model for the Cr composition fluctuations that we will use in this paper to describe their evolution during aging [95]. It shows the absence of significant evolution of the softening reverted austenite and the hardening Cu-rich precipitation during aging. It also shows that Ni, Mn and Si-rich phase appears in two different ways. Finally, it gives a full description of the Fe-Cr matrix unmixing with a phenomenological model based on the aging parameters and shows that in this study the material's hardness increase was found to be proportional to the evolution of the Cr composition fluctuations' amplitude resulting from the unmixing.

2. Experimental procedure

Before the current investigation, the 15-5PH alloy, whose composition is given in Table 1, was subjected to a solutionizing treatment around 1000°C for about 80 min before air quench followed by a precipitation heat treatment of 5h at 505°C. It was supplied by Aubert & Duval.

	Cr	Ni	Cu	Mn	Si	Mo	Nb	C	P	S	Fe
%wt	14.87	4.93	2.99	0.8	0.38	0.27	0.21	0.025	0.019	<0.002	bal.
%at	15.85	4.65	2.61	0.81	0.75	0.16	0.13	0.115	0.034	<0.004	bal.

Table 1: Chemical composition of the 15-5PH alloy under study

The material was then aged for different durations up to 15000 hours at 290°C, 325°C and 350°C, up to 5000 hours at 370°C and 400°C and up to 500 hours at 420°C.

In order to achieve the characterization of the diverse elements of the microstructure, we used complementary techniques:

- Atom Probe Tomography (APT) to characterize the composition of the nanometer size precipitates and the composition fluctuations appearing during aging due to the matrix decomposition.
- Small-Angle X-ray and Neutron Scattering (SAXS and SANS) to characterize the size and volume fraction (or compositional fluctuations' amplitude) of these elements of the microstructure.
- Precession Electron Diffraction (PED) in the Transmission Electron Microscope (TEM) to characterize the size, localization and morphology of the phases at the sub-micron scale (austenite and ferrite).
- X-Ray Diffraction (XRD) to determine the austenite's volume fraction.

In addition, the changes in mechanical behavior were monitored by measuring the evolution of the Vickers microhardness (HV) of the alloy during aging.

APT samples were prepared from parallelepipeds 0.2 x 0.2 x 15 mm^3 using the two-step electro-polishing procedure described in [78] with a mixture of 5% perchloric acid in acetic acid for the first step and a mixture of 2% perchloric acid in 2-butoxyethanol for the second step. For these experiments, we selected different aging times at 350°C (1000h, 2000h, 5000h, 10000h, 12000h, 15000h) to characterize the evolution of the microstructure changes at this temperature, as well as the condition aged 5000h at 400°C in order to compare the changes occurring after 5000h at a higher temperature, and the as-received condition as the reference microstructure. The experiments were conducted on a LEAP 3000X HR instrument at the IM2NP laboratory, Marseille, France. We used the laser mode of this instrument (wavelength 532 nm) with an energy varying from 0.6 nJ to 0.2 nJ and an evaporation rate up to 1% at a temperature of 40 K.

SAXS samples were prepared from 0.3 mm sheets thinned down to about 40 µm ± 20 µm by mechanical polishing for all the aged conditions studied and for the as-received condition. The experiments were conducted at the D2AM beamline (BM02) of the European Synchrotron (ESRF) using an X-Ray energy of 5.983 keV just below the Cr absorption edge in order to enhance the contrast between the chromium and iron atoms (anomalous effect). The images recorded on a 2D-CCD camera were corrected for electronic noise, spatial distortion, pixel efficiency and background noise. The obtained signal being isotropic, we performed an azimuthal average of the images, obtaining the integrated intensity over a range of scattering vectors [$3\text{x}10^{-2}$ Å^{-1}, $6\text{x}10^{-1}$ Å^{-1}]. The intensity was normalized by measuring the transmission of each specimen and of a glassy-carbon reference sample [79].

SANS samples were parallelepipeds 3 x 10 x 15 mm^3 for the different aging times up to 500 h at 420°C, 2250 h at 400°C, 5000 h at 370°C and 6250 h at 290°C, 325°C and 350°C. The experiments were conducted at the D11 beamline of the Institut Laue-Langevin (ILL) using neutrons of wavelength of 4.6 Å (above Bragg cut-off) and a saturating magnetic field of 1.6 T applied to the samples. Two sample-to-detector distances of 1.6 m and 8 m were used. The obtained images were corrected for pixel efficiency and background noise. The magnetic contrast was separated from the isotropic nuclear contrast using a fit of the corrected scattered intensity of the form $sin^2\psi$ where ψ is the angle relative to the direction of the magnetic field vector [80]. The two obtained scattered intensities originating from the scattering by the nuclei of the atoms and by their magnetic moment covered a q range of [$1.6\text{x}10^{-2}$ Å^{-1}, $4.5\text{x}10^{-1}$ Å^{-1}]. The intensity was normalized by measuring the transmission of each specimen and the intensity of the direct beam through calibrated filters.

The TEM samples used for phase and orientation mapping were prepared from 0.3 mm thick sheets thinned down to 80 µm by mechanical polishing for the as-received condition and after aging 5000 h at 400°C and 10000 h at 350°C. The thinned sheets were then cut into 3 mm diameter disks and electropolished using a double jet TenuPol 5 apparatus with a mixture of 10% perchloric acid, 20% 2-butoxyethanol and ethanol at 2°C under 14 V voltage. The experiments were conducted on a Jeol 3010 instrument coupled with a PED technique using the ASTAR package, providing crystallographic orientation and phase maps with a step size of 15 nm of a selected area of the sample [81,82].

The XRD experiments were conducted on a PANalytical X'PERT MPD instrument equipped with a 1D detector and a cobalt source (wavelength 1.789 Å). The diffracted intensity was recorded over a 2θ range [45°, 130°] containing the {110}, {200}, {211} and {220} peaks of the martensitic matrix and the {111}, {200}, {220}, {311} and {222} peaks of the austenite. The austenite's volume fraction for the different tested aging conditions was calculated using a Rietveld analysis of the data, using the Fullprof software. The samples used for the XRD experiments were polished with a colloidal alumina dispersion (0.04 µm) to minimize the depth of surface work-hardening thereby increasing the separation of the {110} martensite and {111} austenite peaks.

Hardness measurements were carried out on a Tukon 1102 Wilson Hardness tester with a Vickers indenter, using a 1 kgf load and a 10 s dwell time. The value for each aging condition is the average of 60 measurements on the same sample. The samples used for the hardness measurements were polished in the same way as for X-ray diffraction.

3. Results

3.1. Austenite

Figure 1 shows phase maps obtained in the TEM, in the as-received condition and two aged conditions (10000h at 350°C and 5000h at 400°C). The corresponding orientation maps can be found in the supplementary material. These phase maps show little evolution of the localization of the austenite islands that were present in the as-received condition. In addition to a tendency to become more equiaxed, these zones are systematically found at crystallographic interfaces, either prior austenite grain boundaries or martensite lath boundaries.

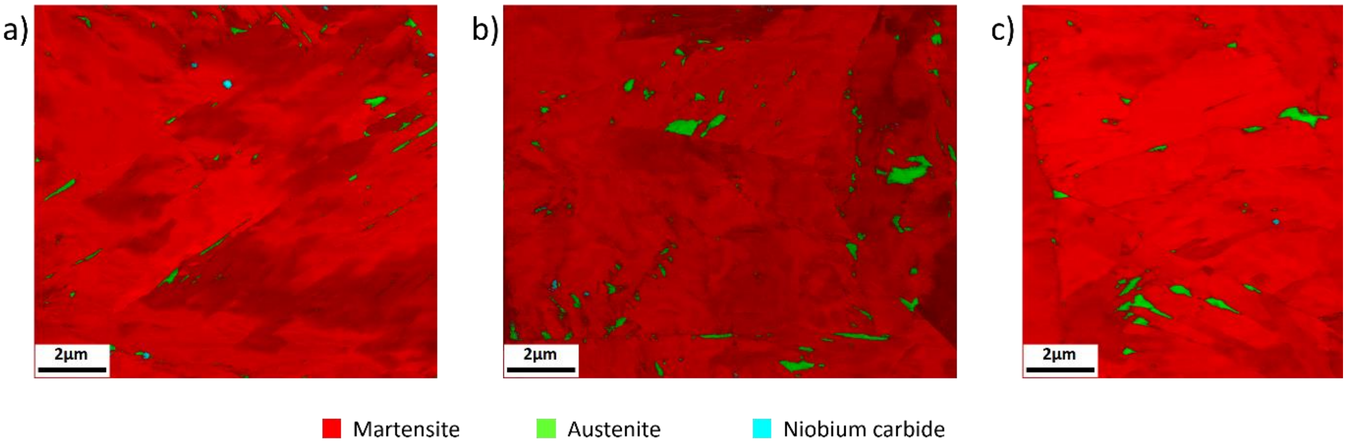

Figure 1: Phase maps showing the localization and aspect of the austenite islands (in green) for three conditions: a) as received, b) 10000h@350°C and c) 5000h@400°C. The grey scale in the images' background indicates the reliability of the PED indexation (white = good, black = poor).

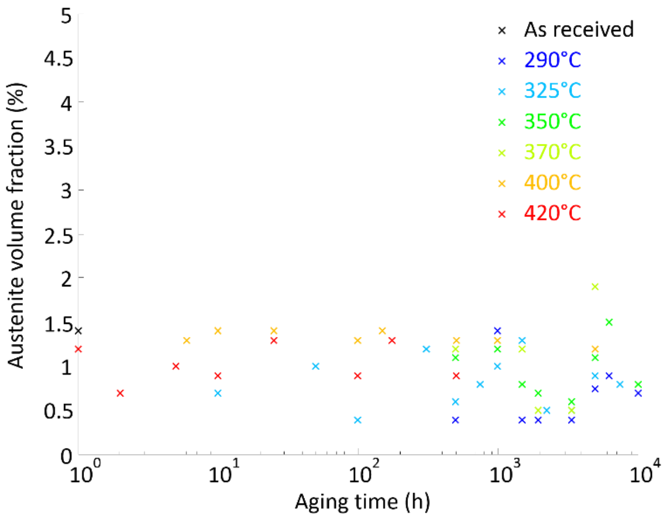

Figure 2: Evolution of the austenite's volume fraction during aging (semi-log) at six different temperatures ranging from 290°C to 420°C measured by XRD.

Figure 2 represents the austenite's volume fraction measured by XRD for the various tested aging conditions. Irrespective of the aging time, the fraction is measured at 1 ± 0.5%, showing no significant evolution even for the longest investigated aging times.

3.2. Copper precipitates

Precipitate composition

Figure 3 shows the distribution of Cu atoms and 10 at% isosurfaces in APT reconstructions of the as-received material and the material aged 15000h at 350°C. Qualitatively, aging does not result in a drastic change of the copper precipitates distribution.

Proxigrams have been calculated on the 10 at% isosurfaces defining the precipitates. These are represented in Figure 4. We have already shown in our previous work [83] that the copper precipitates ensuring the hardening of this 15-5PH steel have a core-shell structure composed of a copper-rich core and a shell rich in nickel, manganese and silicon, which according to literature is reducing the interface energy of the copper precipitates [84–86]. The Cu profiles of the two proxigrams (as-received and aged) are remarkably similar, except for the measurement points at the deepest core (most negative x-values), which represent only the composition of the very few largest precipitates in the measured volume. The Cu content in the precipitate core is larger than 80% and decreases progressively to reach the matrix value close to the interface.

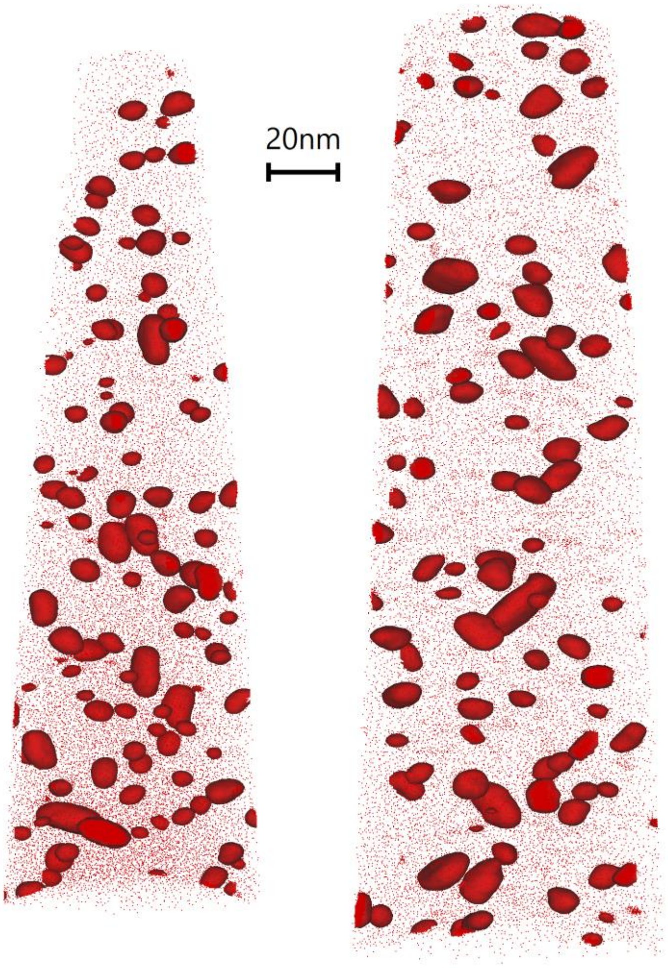

Figure 3: APT reconstructions of the as-received (left) and aged 15000h@350°C (right) where are displayed 10at% Cu isoconcentration surfaces (Cu precipitates) together with 25% of the total Cu atoms.

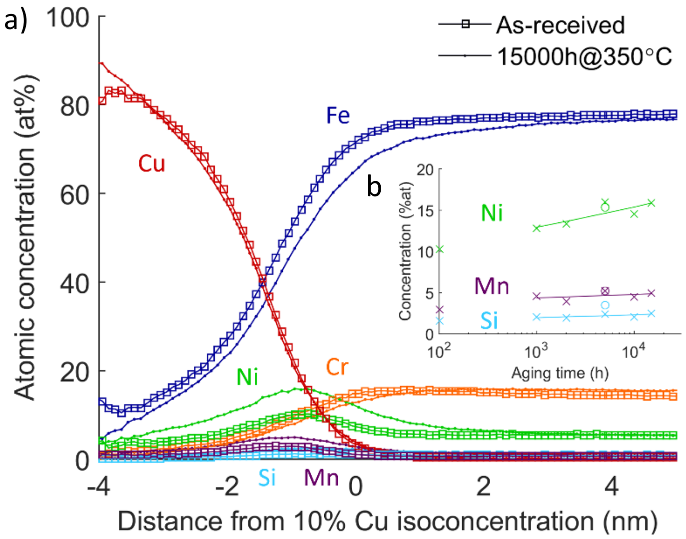

Figure 4: a) Comparison of the proxigrams computed on surfaces of 10at% copper isoconcentration for the as-received and aged 15000h@350°C material. The insert b) shows the evolution of the maximum concentration of nickel, manganese and silicon measured in the copper precipitates shells during the aging at 350°C.

However, the precipitate shells undergo a significant enrichment in Ni, Mn and Si during aging at 350°C. The local maximum of the composition of these three elements in the shell is plotted vs. aging time at 350°C in the inset of Figure 4, showing a clear increase of the Ni content, and to a smaller extent of the Mn and Si content at the Cu precipitates interface.

Matrix composition and precipitate volume fraction

The Cu composition of the matrix C_m was measured using the first nearest neighbor distribution (1NND) of Cu atoms analyzed according to the DIAM method proposed by De Geuser and Lefebvre [87]. From the measurement of the matrix composition, assuming an equal atomic volume of the matrix and the precipitates, a mass balance on the Cu atoms makes it possible to determine the volume fraction f_v of the Cu precipitates:

$$f_v = \frac{C_0 - C_m}{C_p - C_m} \tag{1}$$

Where C_0 is the average Cu composition of the alloy and C_p is the Cu composition in the precipitates. As we have seen above, the Cu composition in the precipitates can be assumed to be constant during aging, so we used a unique value for C_p, which we calculate by integrating the Cu composition from the precipitate core to the inflection point of the Cu concentration gradient close to the precipitates interface, corresponding to about 40 at%, for the proxigram obtained on the largest analyzed volume. We obtained for C_p 59 at% and we used for C_0 the nominal composition of 2.61 at%. While the choice of these two values is arguable and may affect the absolute values of volume fraction, we do not expect them to affect the obtained trends and magnitudes.

Figure 5 presents the evolution of the Cu precipitates' volume fraction and the Cu matrix composition during aging at 350°C. This data shows that the matrix concentration is constant, and that consequently the volume fraction is constant at 3.9 ± 0.1%, even for durations as long as 15000 h.

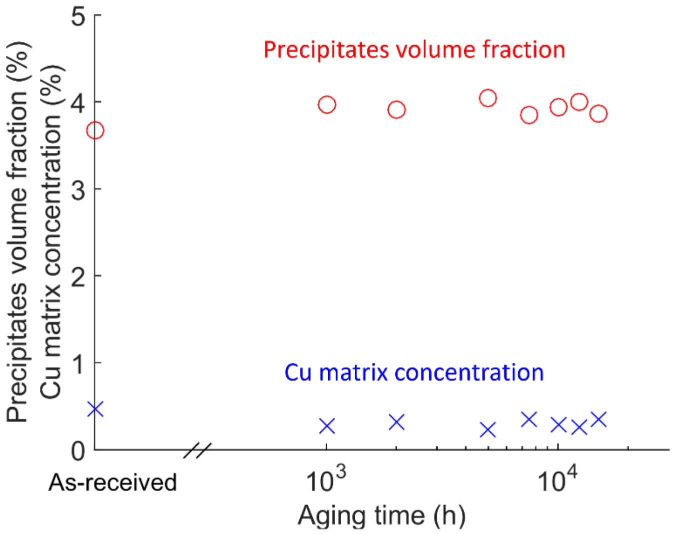

Figure 5: Evolution of the copper matrix concentration (blue crosses) and of copper precipitates' volume fraction (red circles) during the aging at 350°C.

Precipitate size

The mean radius of the precipitates and the corresponding integrated intensity of the copper precipitates were measured from the small-angle scattering (SAS) data as explained in our previous work [83].

The evolution of the mean radius of the precipitates can be determined using three sets of data: SAXS data where the contrast originates from fluctuations in electron density, nuclear SANS data where the contrast originates from fluctuations in nuclear scattering length density, and magnetic SANS data where the contrast originates from fluctuations in magnetic moment. The absolute values of the mean radii determined by these three methods appeared to be slightly different. These discrepancies can be attributed to the presence of the shell around the copper precipitates.

The shell is enriched in Ni and Mn, which have a different neutron scattering length from that of Cu and from that of the matrix, 10.3 fm, -3.73 fm, 7.72 fm and 9 fm respectively [88]. Thus the shell constitutes a distinct entity for SANS from the viewpoint of the nuclear contrast. Therefore, the interpretation of this dataset would require a more elaborated model for the description of the intensity scattered by the copper precipitates such as the one proposed by Mathon et al. [89].

In the case of X-rays, the shell has a mean electron density close to that of the matrix, 23.0 electrons/atom and 23.4 electrons/atom respectively. Thus, we can consider that for X-rays, we have pure Cu precipitates embedded in a 0.8Fe-0.15Cr-0.05Ni matrix.

In the case of SANS with magnetic contrast, if we assume that the shell is non-ferromagnetic or only weakly ferromagnetic, the scattering domains are composed of the core of the precipitates plus at least a part of their shell and so they should appear slightly larger than in the case of X-rays where the intensity scattered by copper precipitates corresponds only to the precipitates cores. Considering this, the X-ray data seems more reliable for the characterization of the size of copper precipitates. However, for the long aging times, the relatively intense signal scattered by the Fe-Cr unmixing is significantly overlapping with the signal originating from the copper precipitates. Thus, we will only present here the characterization of the copper precipitates evolution obtained using the neutrons' magnetic contrast, whose values are shown in Figure 6. No significant evolution of the precipitates radius was found at any aging time and temperature, confirming the local observations made in the APT data sets for a few aging conditions.

The interpretation of the integrated SAS intensity that classically leads to the determination of volume fraction of precipitates [90,91] will not be directly commented here, due to the complex evolution of the precipitate shell and to the appearance of the G phase during aging (see next section), which prevent a simple interpretation and would not provide additional information from that of the volume fraction determined from APT measurements.

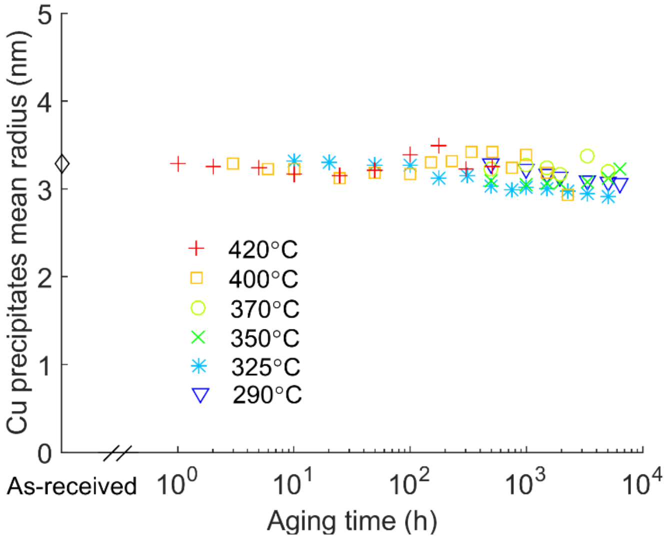

Figure 6: Evolution of copper precipitates mean radius for the aging at six different temperatures ranging from 290°C to 420°C.

3.3. G phase

Composition and spatial distribution of Ni, Si and Mn-rich precipitates

Figure 7 shows 15 nm thick slices of APT reconstructions with the same 10 at%Cu isosurfaces to represent the Cu precipitates, and Si atoms represented in blue, for different aging times at 350°C and one aging time at 400°C.

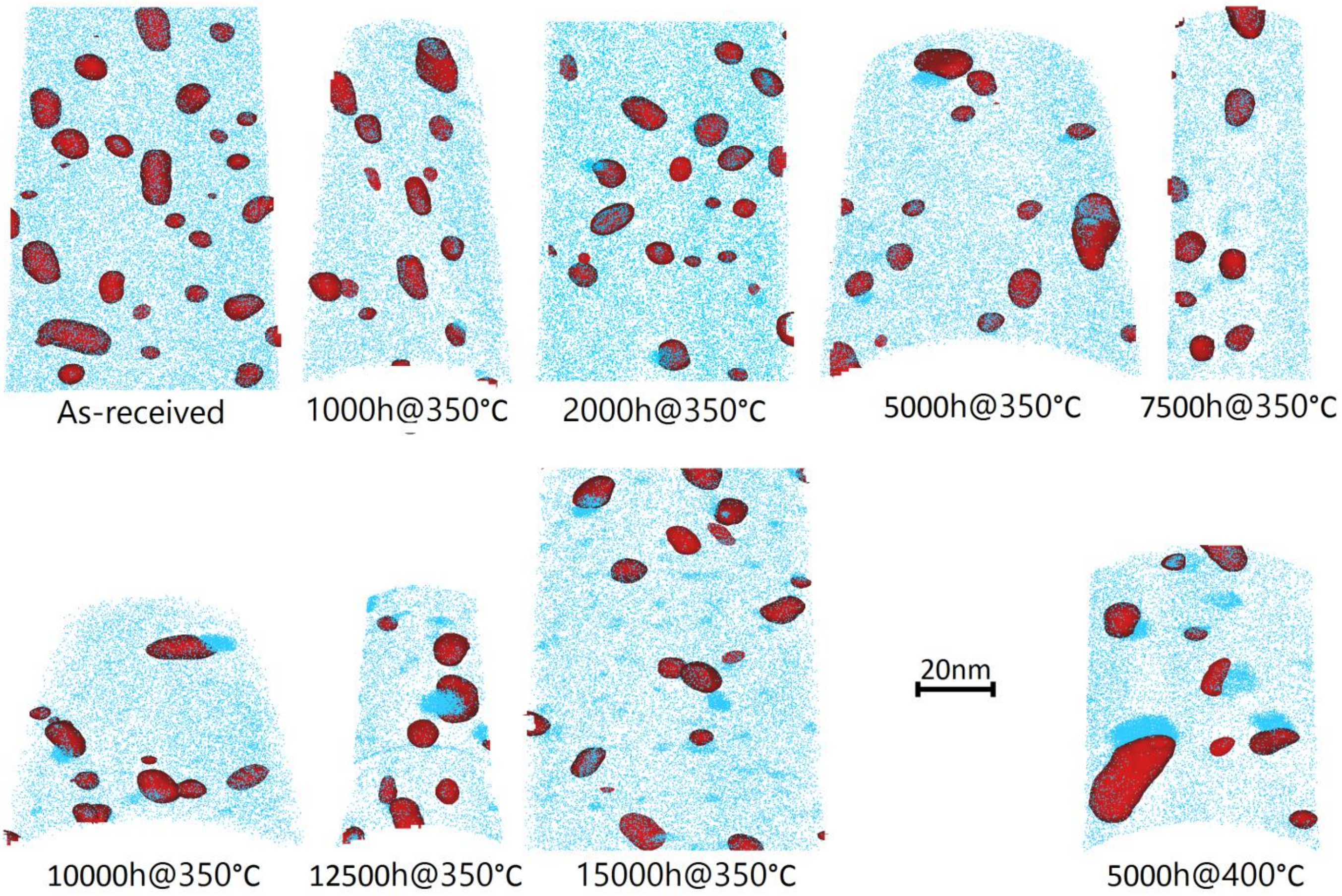

Figure 7: Evolution of the silicon atoms (blue points) spatial distribution during aging. Illustration of the silicon rich precipitation on the copper precipitates (red surfaces) and later in the matrix.

These datasets show that Si-rich precipitates appear during aging at 350°C. At first, they form at the copper precipitates interfaces, as can be observed first on the 1000 h at 350°C dataset. This precipitation continues to nucleate and grow at the copper precipitates interfaces. At longer aging times, however, one can additionally observe nucleation of Si-rich precipitates within the matrix in-between the copper precipitates. These tiny particles dispersed within the martensitic matrix seem to appear around 10000 h and one can very clearly see them after 12500 h.

In addition to their location (at the interface of the Cu precipitates or homogeneously dispersed), these precipitates also differ in size and composition. Using the proxigram tool for APT analysis, we measured the compositions of these two kinds of Si-rich phases in the dataset obtained after 15000 h aging at 350°C. The results are presented in Table 2. One can observe from these measurements that the large precipitates, nucleated on the Ni, Mn and Si-rich shell of the Cu precipitates, have a composition corresponding to the reported G-phase stoichiometry $Mn_6Si_7Ni_{16}$ [92,93,29,30,32]. Although we lack a structural characterization of these particles, it is highly likely that they correspond to G-phase. On the other hand, the smaller precipitates homogeneously distributed within the matrix have a very different composition. They contain high proportions of the matrix elements Fe and Cr, they present a Ni/Mn ratio slightly higher but close to that of the G-phase stoichiometry, but their Ni/Si ratio of 5.0 is significantly higher than that of $Mn_6Si_7Ni_{16}$, namely 2.3.

	Ni	Si	Mn	Fe	Cu	Cr
Large precipitate (heterogeneous precipitation)	52%at	24%at	19%at	4%at	1%at	0%at
Small precipitates (homogeneous precipitation)	25%at	5%at	8%at	52%at	2%at	8%at

Table 2: Measured concentrations (APT) of the G-phase precipitates in the material aged 15000h at 350°C. The first line corresponds to one large precipitate heterogeneously nucleated on a copper precipitate and the second line to ten small precipitates homogeneously nucleated in the matrix.

Estimated volume fraction from SANS

The characterization of the G-phase precipitates volume fraction is non-trivial via SAS techniques. Firstly, since these precipitates have a similar size as compared to the copper precipitates, they give rise to scattered intensity in the same q-range. Secondly, the electron density contrast of the G-phase precipitates, with the surrounding matrix is very weak, preventing its characterization by SAXS.

For the magnetic SANS data interpretation, we assumed that the G-phase is paramagnetic. This hypothesis seems reasonable at least for the large precipitates with a low Cr and Fe content. It is further supported by the fact that the magnetic SANS integrated intensity increases with aging time while APT measurements showed that the volume fraction of Cu precipitates is constant during aging. This indicates that non-magnetic precipitates, which are not Cu-rich precipitates but with a similar size, appear progressively during aging. According to our APT observations these have to be the G-phase precipitates. So, to convert the magnetic SANS integrated intensity into the volume fraction of G-phase precipitates, we supposed that Cu-rich and G-phase precipitates have the same neutrons' magnetic contrast with the surrounding matrix considered as a Fe-0.15Cr mixture. According to Aldred [94], such a Fe-Cr mixture presents a bulk magnetic moment of $1.837\mu_B$ while the magnetic moment of the precipitates is zero, leading to a neutrons' magnetic contrast of $1.75 \times 10^{21} cm^{-4}$. Based on the hypothesis of a constant Cu-rich precipitates' volume fraction, the G-phase precipitates' volume fraction can be estimated by subtracting for each aging condition the integrated intensity measured in the as-received sample that corresponds to the copper precipitates only. Using this methodology, the evolution of the estimated G-phase volume fraction during aging between 290°C and 420°C is displayed in Figure 8.

Since this estimation of G-phase volume fraction is indirect, we verified that the obtained estimates are realistic values. In order to do so, we computed the maximum volume fraction that could be achieved in the studied alloy. Considering the material nominal composition in Table 1 and the G-phase stoichiometry, Si is the limiting reactant of the G-phase precipitation, allowing to write the mass balance:

$$C_0^{Si} = C_{ppt}^{Si} f_v + C_m^{Si}(1 - f_v) = C_{ppt}^{Si} f_v \qquad (2)$$

Where f_v is the G-phase volume fraction, C_0^{Si}, C_{ppt}^{Si} and C_m^{Si} are the Si contents in the alloy, precipitates and matrix respectively. Once again we assumed here the atomic volumes of matrix and precipitates to be equal. Furthermore, we made the 2 following hypotheses:

- the lattice parameter of the cubic unit cell of G-phase, which contains 116 atoms, is four times the one of the body centered cubic martensitic matrix [24],
- the Si content C_0^{Si} is equal to the nominal Si content in the alloy.

the maximum G-phase volume fraction based on these hypotheses is about 3.4%, which is indeed larger but of the same order of magnitude than all measurements from SANS data (maximum of 2.5%).

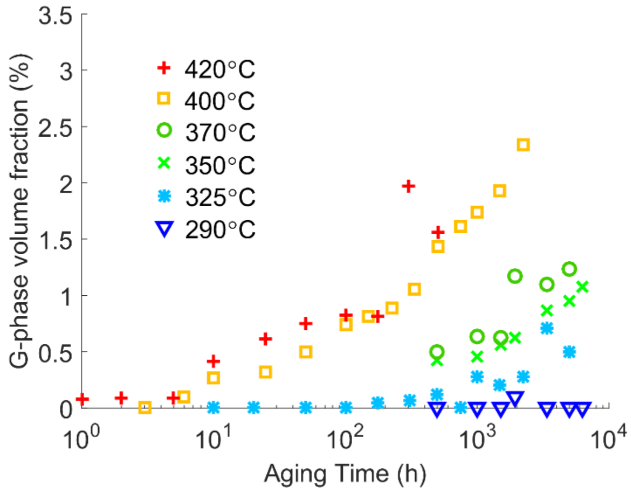

Figure 8: Evolution kinetics (semi-log) of G-phase volume fraction indirectly determined using SANS data (magnetic contrast).

3.4. Fe-Cr unmixing

We studied the evolution of the Fe-Cr unmixing of the matrix using SAS techniques and APT. Among the different acquired SAS signals, we will only present in this section the SAXS results. Indeed, the X-ray contrast is the one allowing the best separation between the intensities scattered by the precipitates (Cu-rich and G-phase) and the Fe-Cr unmixing. APT results have already been presented in a previous study [95] and compared to SAXS results, showing a good agreement. They will not be presented again.

To describe Fe-Cr unmixing we used a three parameters model of the autocorrelation function of the Cr atoms distribution $\gamma(r)$ introduced in our former work [95] that can be translated in a small-angle scattering signal fitted on the experimental data:

$$\gamma(r) = K\frac{A^2}{2}cos\left(\frac{2\pi r}{\lambda}\right)exp\left(-\frac{r}{\xi}\right) \tag{3}$$

In equation (3), K is a constant related to the X-ray contrast and the three parameters of the model are the mean amplitude A, the mean wavelength λ and the correlation length ξ of the Cr composition fluctuations within the material. As discussed in our previous article [95], the parameter ξ, which characterizes the width of the Cr composition fluctuations, has a predominant influence on SAXS signal (via the shape of the autocorrelation function) over that of the mean wavelength λ. Thus, in the following, we will only present and discuss the evolution of the Cr composition fluctuations amplitude and correlation length measured in SAXS. The raw SAXS data along with the fit of the model by equation (3) can be found in the supplementary material.

The two graphs on Figure 9 present the evolution during aging kinetics of the amplitude and correlation length obtained for the six studied temperatures. As expected, both parameters increase with aging time and the kinetics accelerates with increasing aging temperature. An interesting point to notice is that both parameters have non-zero values in the unaged condition, meaning that all Cr atoms are not in homogenized solid solution in this condition. A possible explanation for this non-zero amplitude and correlation length, based on our microstructure observations, will be discussed below. Alongside with the data points, we draw on these graphs a fit for each aging temperature that is a power law of aging time.

Considering the two graphs in Figure 9, one can immediately observe that the amplitude increases more rapidly than the correlation length, especially for the lowest aging temperatures. Also, the effect of aging temperature seems more important on correlation length, going from almost no evolution for aging at 290°C to a rapid increase at 420°C, whereas the acceleration of amplitude increase is less marked for the same aging temperature interval.

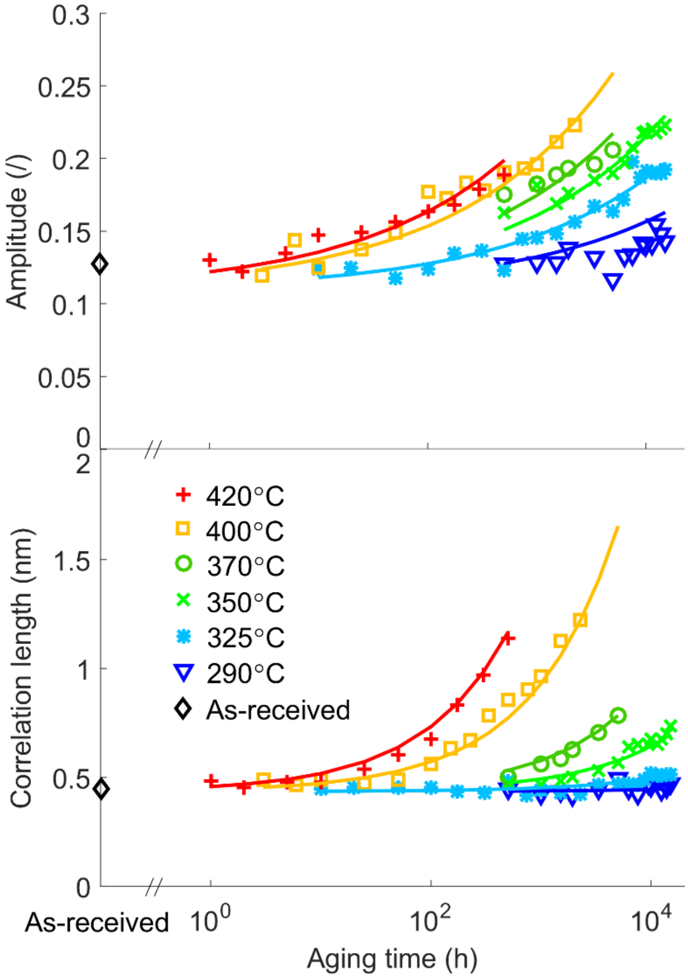

Figure 9: Evolution kinetics (semi-log) of the amplitude (top) and correlation length (bottom) of the chromium fluctuations measured in SAXS compared to the values measured in the as-received state (in black). Solid lines are guides for the eyes.

3.5. Material hardness

The effect of aging on the mechanical properties has been monitored by measuring the Vickers microhardness evolution at the six aging temperatures. The obtained results are gathered in

Figure 10 together with the as-received microhardness. As expected, one observes a rapid and significant increase of hardness with aging time even for the lowest aging temperature. In addition, the microhardness increase is accelerating for increasing aging temperature.

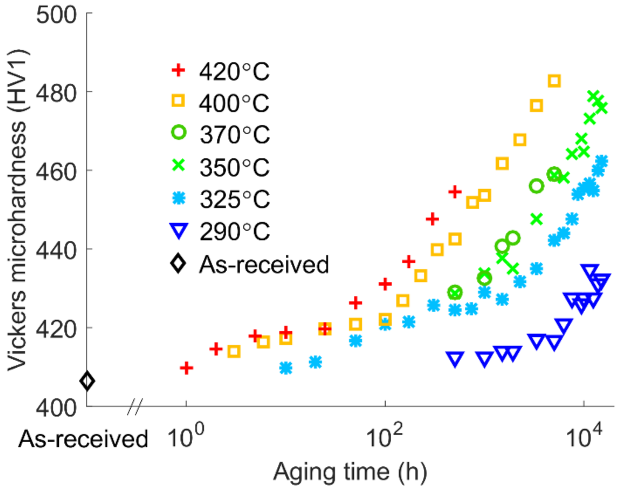

Figure 10: Vickers microhardness evolution kinetics (semi-log) at six different aging temperatures ranging from 290°C to 420°C compared to the microhardness in the as-received state (in black).

4. Discussion

4.1. Minor evolution of austenite and copper precipitates

Firstly, one can conclude from the data presented in Figure 1 and Figure 2 that during aging at any studied temperature the only significant evolution of the austenite is a slight change in its aspect ratio toward more equiaxed austenite islands. These islands remain located at the crystallographic interfaces and keep a constant volume fraction of 1 ± 0.5%.

Secondly, the results obtained on the Cu-rich precipitates show that they also undergo only a slight evolution during aging. SAS results (Figure 6) show that no significant evolution of the Cu precipitates size is observed, their mean radius remaining almost constant around 3 nm. In addition, APT results (Figure 5) show that no significant evolution of the Cu matrix concentration and precipitates volume fraction is observed either, the latter remaining constant slightly below 4% during the aging at 350°C. These two conclusions may also be visualized on the two APT datasets presented in Figure 3 where it can be seen that Cu precipitates seem not to exhibit major differences in size and spatial distribution between the as-received material and the one aged 15000 h at 350°C. Finally, based on the APT proxigrams presented in Figure 4, it seems that the only significant evolution of the Cu-rich precipitates during aging at 350°C is an increase in the Ni, Mn and Si content of their shell, the core composition remaining constant. To understand this observed increase, one has to consider the observations made on the APT results presented in Figure 7 showing the rapid precipitation of Si-rich precipitates directly on Cu-rich precipitates. Since the proxigram analysis is averaging the composition profiles measured all around the precipitate(s) considered for calculation, the observed increase might simply be due to the nucleation and growth of these Si-rich precipitates that also present high Ni and Mn contents, as reported in Table 2.

4.2. Heterogeneous and homogeneous G phase precipitation

As mentioned in section 3.3, the high similarity between the measured composition of the Si-enrichments around the Cu precipitates and the stoichiometry of the G phase tends to indicate that G phase precipitates nucleate in a heterogeneous manner on the shell of the Cu precipitates. This kind of heterogeneous nucleation of G phase on a Ni and/or Mn rich shell of Cu precipitates has already been observed in other stainless steels [5,13–15] and heterogeneous nucleation on dislocations has also been reported [22,23]. The heterogeneous nucleation of G-phase on the Cu precipitates may be explained by the presence of the Ni, Mn and Si rich shells around these. These 3 elements are the constituents of the G-phase and their relatively high concentration in the vicinity of the Cu precipitates leads to the rapid formation of stable nuclei of G-phase. In addition, Ni and Mn segregation around the Cu-rich precipitates in stainless steels has been observed and explained by a decrease of the precipitate/matrix interface energy due to Ni and Mn [96,85,84,86]. Yeli et al. recently developed an interesting theory about the role of Nb in the precipitation sequence of G-phase like precipitates in 17-4PH [14], but, unfortunately, we were not able to see any correlation between Nb distribution and Cu or G-phase precipitation in our study. This may be because of the lower Nb content detected in our APT data sets, less than 0.03%at in average, making Nb segregations more difficult to observe.

As reported in section 3.3, the homogeneous Ni, Mn and Si rich clusters that appear later during aging, after approximately 10000 h at 350°C, have a different composition from that of the large particles nucleated on the Cu precipitates. Especially, they still contain a large amount of matrix elements, namely Fe and Cr, although this might be an APT artifact [97,98]. Nonetheless, even if we leave this high concentration in matrix elements aside, we can still notice that the Ni/Si ratio is almost twice the ratio measured in the larger precipitates (Table 2). The Ni/Si, Ni/Mn and global cluster composition measured here is compatible with the values reported in the recent study from Matsukawa et al. for G-phase clusters (less than 3nm) nucleating in the ferrite phase of duplex stainless steel during aging at 400°C [22]. According to this study, one can suppose that these clusters have not yet the G-phase structure since Matsukawa claims that the clusters have to reach a composition close to $Ni_{16}Si_{3.5}(Fe,Cr)_{3.5}Mn_6$ to go through the structural transformation leading to the cF116 G-phase crystallographic structure with a lattice parameter being four times that of bcc ferrite [22]. These clusters may then be considered as precursors of the G-phase.

A theory for the nucleation of these G-phase precursors has been proposed by Mateo et al. [24]. These authors proposed that the local enrichments in Ni, Mn and Si leading to nucleation of G-phase precursors are caused by the Fe-Cr unmixing. Indeed, during the Fe-rich and Cr-rich zones formation, Ni and Mn atoms are rejected from the Cr-rich zones and Si atoms are rejected from the Fe-rich zones meeting at the interdomains. This mechanism would explain the correlation between G-phase precipitation and Fe-Cr unmixing evolutions that has been observed many times in aging of stainless steels [32,34,35,39,40,52,99].

This co-evolution of G-phase precipitation and Fe-Cr unmixing makes it difficult to separate the role of G-phase on the mechanical properties evolution of stainless steels during aging. In some research works the effect of G-phase on mechanical properties is reported as negligible compared to the one of Fe-Cr unmixing, considered as the main responsible for properties change [5,28,33] and in others, it is claimed that G-phase had an important role in the material hardening [34,35]. Although, a very recent work by Badyka et al. seems to prove that in many cases G-phase may play an important role in the material hardening during aging [12]. But the respective part of each mechanism in the properties evolution depends on the material under study and the aging conditions. In our study, we did not intend to separate the contributions of G-phase and Fe-Cr unmixing and we will show in the following that one can establish a direct correlation between the Fe-Cr unmixing characteristics and the materials hardness evolutions, keeping in mind that this correlation does not rule out an effect of the G-phase on hardening.

4.3. Kinetics of Fe-Cr unmixing and correlation with hardness

As stated previously, we were able to successfully describe the Cr composition fluctuations' amplitude and correlation length with empirical power laws of the aging time for each aging temperature as one can see on the two graphs presented in Figure 9. This model for the Fe-Cr unmixing characteristics evolution has the form:

$$P = P_0 + (k_P(T).t)^{a_P} \tag{4}$$

Where P is the considered Fe-Cr unmixing parameter (amplitude or correlation length), P_0 is the value of this parameter in the unaged state, t is the aging time. For both the amplitude and the correlation length, a single time exponent a_P can be found to describe the six measured kinetics, namely 0.31 and 0.56 for amplitude and correlation length respectively.

For both characteristics, it was found that the power-law pre-factor k_P can be described as an Arrhenius function of aging temperature T leading to the determination of an activation energy for each Fe-Cr unmixing characteristics evolution: 126kJ.mol^{-1} for amplitude and 269kJ.mol^{-1} for correlation length (see supplementary material for the Arrhenius plots). The activation energy value found for the Cr composition fluctuations' correlation length agrees with the activation energy of Cr diffusion in ferrite, which lies around 240kJ.mol^{-1} [100–102]. This is also the order of magnitude of the activation energy usually associated with Fe-Cr unmixing in the literature since this phenomenon is usually controlled by Cr diffusion in ferrite [8,12,41,65,103–106]. Conversely, the value obtained in our study for the Cr composition fluctuations' amplitude evolution may appear surprisingly low. One major difference between our study and the previous works where activation energy values have been determined is the nominal Cr concentration of the material under study. Indeed, the 15-5PH has a rather low Cr content compared to binary alloys or ferrite of duplex steels, which are usually used for the Fe-Cr unmixing studies. Thus, our hypothesis to explain the low activation energy measured for the amplitude evolution is that it is not controlled by Cr diffusion alone but also by the unmixing driving force. Considering the rather low Cr content of 15-5PH steel and the studied aging temperature interval, this driving force must be quite low and highly temperature-dependent, leading to an apparent decrease of the activation energy for amplitude evolution.

The existence of a single value of activation energy Q over the whole studied aging temperature interval for each Fe-Cr unmixing characteristics allows the use of a simplified representation of the results: an equivalent aging time. This equivalent aging time ${t_{eq}}_{T_{eq}}$ at an arbitrary chosen equivalent aging temperature T_{eq} can be expressed as follows:

$${t_{eq}}_{T_{eq}} = t.exp\left(-\frac{Q\left(T_{eq} - T\right)}{R.T.T_{eq}}\right) \tag{5}$$

Where t is the aging time at an aging temperature T and R is the gas constant. We used this with the two reported activation energies determined for amplitude and correlation length evolutions at an equivalent aging temperature of 350°C to draw the two graphs presented in

Figure 11. On these two graphs, one can notice that all the measured amplitudes (Figure 11 top graph) and correlation lengths (Figure 11 bottom graph) are gathered along a master curve, which equation is of the form of equation (4), where k_P is now a constant, since we consider a single equivalent aging temperature.

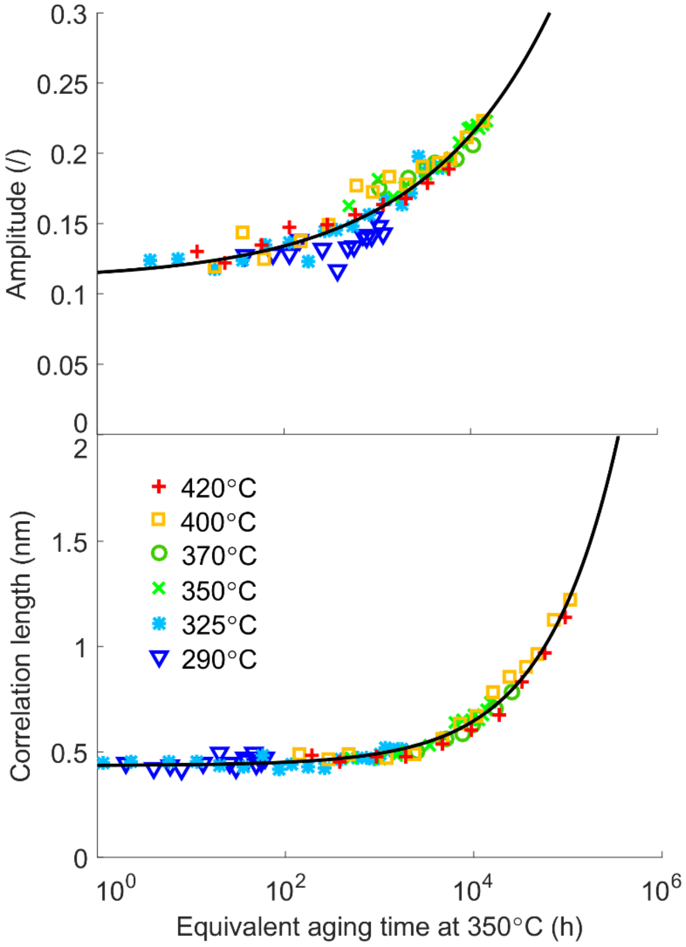

Figure 11: Amplitude (top graph) and correlation length (bottom graph) data points obtained for the aging at the six studied temperatures gathered on a single master curve using an activation energy to compute an equivalent aging time at 350°C (semi-log).

The values of the time exponent a_P obtained by fitting the data in the equivalent time representation are 0.31 for the amplitude and 0.56 for the correlation length. One can find in the literature many descriptions of Fe-Cr unmixing evolution using a power law of the aging time and thus many different values of the time exponent [39,52–72]. Among these studies, there are both experimental and modeling works but most of them are concerned with the description of the characteristic size of the Fe-Cr unmixing, which in our work is the correlation length of the Cr composition fluctuations, and only a few of them consider the amplitude evolution. All the reported time exponents are in a wide interval, [0.07 – 0.35]. One can notice that the time exponents determined in the present work are close to the upper limit of this interval in the case of amplitude kinetics and above this upper limit in the case of the correlation length kinetics. This may indicate that the mechanism of the observed Fe-Cr unmixing is closer to the nucleation and growth than to the spinodal decomposition one, since a vast majority of the time exponent values collected in the literature were obtained for the spinodal decomposition mechanism. But this may also be due to the different model that we used to describe the characteristics evolutions. Indeed, although the works from literature consider only a power-law of aging time, we did consider a power-law added to a constant since we measured non-zero values for both amplitude and correlation length in the initial state of the material under study.

The origin of these non-zero values of amplitude and correlation length determined for the unaged condition, 0.11 and 0.44nm respectively, also needs to be discussed. Pettersson et al. also reported that some Cr segregations can already be seen in the unaged condition in the ferrite of a duplex stainless steel [11]. In addition, we already showed and discussed this non-random distribution of Cr within the material in the as-received state in our previous work [7,95]. An early-stage Fe-Cr unmixing is already present in this state together with some Cr segregation on the dislocations according to our APT observations, which explains the non-zero values measured in SAXS for amplitude and correlation length.

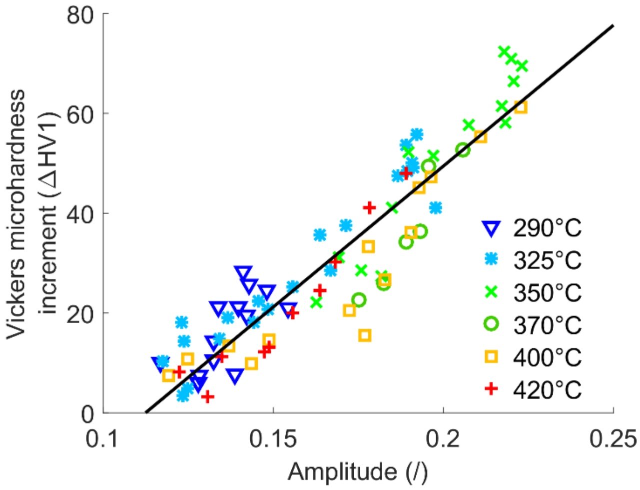

Figure 12: Linear correlation between amplitude of Cr fluctuations and Vickers microhardness increment over aging at all temperatures in the range 290°C - 420°C.

The same approach has been used to analyze the 15-5PH microhardness evolution during aging. We then found the activation energy associated with this mechanical property evolution, which is around 106kJ.mol^{-1}. This value is again much lower than that of Cr diffusion in ferrite but is quite close to the one determined for the Cr composition fluctuations' amplitude. Then, if we compare the evolutions of these two characteristics by plotting one versus the other (Figure 12), one can notice that, for the studied aging conditions in the 15-5PH, there exists a linear correlation between the Cr composition fluctuations' amplitude A and the microhardness increase ΔHV of the material that obeys the phenomenological model:

$$\Delta HV = 564\,A - 63.5 \qquad (6)$$

Such a linear dependence between hardness and Cr composition fluctuations' amplitude has already been reported in the literature [11,104]. It seems quite clear now that this amplitude determines the Fe-Cr unmixing obstacle force to the dislocations propagation, via the lattice parameter and elastic moduli changes between the Fe rich zones and the Cr rich zones according to Pettersson et al. and Kato [11,107]. The interesting point from our study is that this linear correlation exists, while the correlation length follows a different evolution with aging time and temperature. This implies that in the range of conditions explored here, the correlation length does not influence significantly the hardness value. This is interesting in regard to the previous studies of the Fe-Cr unmixing kinetics focusing mostly on length scale rather than amplitude.

5. Conclusions

We have investigated with a combination of advanced experimental techniques the microstructural changes in a precipitation-hardened martensitic stainless steel 15-5PH during long term aging at medium temperatures (290°C – 420°C). The main results can be summarized as follows:

- There are only slight changes in the morphology of retained/reverted austenite and no significant evolution of its volume fraction (around 1%).
- There are no significant changes in the Cu-rich strengthening precipitates, neither in term of size, volume fraction nor composition.
- Precipitates rich in Ni, Mn and Si appear during aging in two ways. Precipitates of a few nanometers heterogeneously nucleate quite early during aging (less than 1000 h at 350°C) at the Cu precipitates / matrix interfaces. According to their composition and the existing literature, these are believed to be G-phase precipitates. For longer aging times (around 10000 h at 350°C) clusters homogeneously appear within the matrix. They are believed to form together with the progression of the matrix Fe-Cr unmixing at Fe-rich and Cr-rich interdomains and to be precursors of G-phase precipitates.
- During aging, the Fe-Cr solid solution progressively undergoes an unmixing process.

We focused on the description of this last microstructural evolution as it is believed to be the main responsible for the mechanical properties change during aging. The Fe-Cr unmixing evolution has been characterized by the evolution of the Cr composition fluctuations' amplitude and characteristic length (correlation length of the fluctuations) within the matrix.

The kinetics of the evolution of these two characteristics has been measured and then described by a unified phenomenological model based on a power law of aging time. An activation energy has been determined for both amplitude and correlation length evolutions. The activation energy for correlation length is close to that of Cr diffusion in ferrite (around 240-270 kJ.mol^{-1}) but the one for amplitude is much lower (around 125 kJ.mol^{-1}). We propose that this low value for amplitude is due to the low Cr content in 15-5PH, resulting in a strong variation of unmixing driving force in the considered temperature range.

Finally, for the studied aging conditions, a linear correlation between the hardness and the Cr composition fluctuations' amplitude has been established that indirectly suggests a lack of influence on hardness of the correlation length.

Acknowledgments

Dr. J. Hugues of CIRIMAT laboratory is thanked for realizing some of the aging heat treatments of this study. Dr. M. Descoins and Dr. D. Mangelinck are thanked for help with the APT experiments. The METSA network is acknowledged for giving access to the APT facilities at IM2NP laboratory. The technical staff of ESRF-D2AM and ILL-D11 beamlines is thanked for technical help during the SAXS and SANS experiments. Dr. B. Malard is thanked for help with the Rietveld analysis of the X-ray diffraction data.

References

[1] E. Herny, P. Lours, E. Andrieu, J.M. Cloué, P. Lagain, Evolution of microstructure and impact-strength energy in thermally and thermomechanically aged 15-5 PH, Proc. Inst. Mech. Eng. Part J. Mater. Des. Appl. 222 (2008) 299–304. doi:10.1243/14644207JMDA190.

[2] W. Jun, Z. Hong, W. Xiao-yong, L. Cong, Q. Shao-yu, S. Bao-luo, The Effect of Long-Term Isothermal Aging on Dynamic Fracture Toughness of Type 17-4PH SS at 350°C, Mater. Trans. JIM. 46 (2005) 846–851.

[3] H.J. Rack, D. Kalish, The strength, fracture toughness, and low cycle fatigue behavior of 17-4 PH stainless steel, Metall. Trans. 5 (2013) 1595–1605. doi:10.1007/BF02646331.

[4] K. Ozbaysal, O.T. Inal, Age-hardening kinetics and microstructure of PH 15−5 stainless steel after laser melting and solution treating, J. Mater. Sci. 29 (1994) 1471–1480. doi:10.1007/BF00368911.

[5] M. Murayama, K. Hono, Y. Katayama, Microstructural evolution in a 17-4 PH stainless steel after aging at 400°C, Metall. Mater. Trans. A. 30 (1999) 345–353. doi:10.1007/s11661-999-0323-2.

[6] B. Yrieix, M. Guttmann, Aging between 300 and 450°C of wrought martensitic 13–17 wt-%Cr stainless steels, Mater. Sci. Technol. 9 (1993) 125–137. doi:10.1179/mst.1993.9.2.125.

[7] L. Couturier, F. De Geuser, M. Descoins, A. Deschamps, Evolution of the microstructure of a 15-5PH martensitic stainless steel during precipitation hardening heat treatment, Mater. Des. 107 (2016) 416–425. doi:10.1016/j.matdes.2016.06.068.

[8] P.J. Grobner, The 885° F (475° C) embrittlement of ferritic stainless steels, Metall. Trans. 4 (1973) 251–260. doi:10.1007/BF02649625.

[9] J. González, F. Gutiérrez-Solana, L. Sánchez, J. Setién, Low-Temperature Aging Kinetics in Cast Duplex Stainless Steels: Experimental Characterization, J. Test. Eval. 25 (1997) 154–162. doi:10.1520/JTE11473J.

[10] H.M. Chung, O.K. Chopra, Kinetics and mechanism of thermal aging embrittlement of duplex stainless steels, Argonne National Lab., IL (USA), 1987. http://inis.iaea.org/Search/search.aspx?orig_q=RN:19055539.

[11] N. Pettersson, S. Wessman, M. Thuvander, P. Hedström, J. Odqvist, R.F.A. Pettersson, S. Hertzman, Nanostructure evolution and mechanical property changes during aging of a super duplex stainless steel at 300°C, Mater. Sci. Eng. A. 647 (2015) 241–248. doi:10.1016/j.msea.2015.09.009.

[12] R. Badyka, G. Monnet, S. Saillet, C. Domain, C. Pareige, Quantification of hardening contribution of G-Phase precipitation and spinodal decomposition in aged duplex stainless steel: APT analysis and micro-hardness measurements, J. Nucl. Mater. 514 (2019) 266–275. doi:10.1016/j.jnucmat.2018.12.002.

[13] P.B. Wells, T. Yamamoto, B. Miller, T. Milot, J. Cole, Y. Wu, G.R. Odette, Evolution of manganese–nickel–silicon-dominated phases in highly irradiated reactor pressure vessel steels, Acta Mater. 80 (2014) 205–219. doi:10.1016/j.actamat.2014.07.040.

[14] G. Yeli, M.A. Auger, K. Wilford, G.D.W. Smith, P.A.J. Bagot, M.P. Moody, Sequential nucleation of phases in a 17-4PH steel: Microstructural characterisation and mechanical properties, Acta Mater. 125 (2017) 38–49. doi:10.1016/j.actamat.2016.11.052.

[15] Z. Wang, H. Li, Q. Shen, W. Liu, Z. Wang, Nano-precipitates evolution and their effects on mechanical properties of 17-4 precipitation-hardening stainless steel, Acta Mater. 156 (2018) 158–171. doi:10.1016/j.actamat.2018.06.031.

[16] D.J.M. King, P.A. Burr, S.C. Middleburgh, T.M. Whiting, M.G. Burke, M.R. Wenman, The formation and structure of Fe-Mn-Ni-Si solute clusters and G-phase precipitates in steels, J. Nucl. Mater. 505 (2018) 1–6. doi:10.1016/j.jnucmat.2018.03.050.

[17] P.D. Styman, J.M. Hyde, D. Parfitt, K. Wilford, M.G. Burke, C.A. English, P. Efsing, Post-irradiation annealing of Ni–Mn–Si-enriched clusters in a neutron-irradiated RPV steel weld using Atom Probe Tomography, J. Nucl. Mater. 459 (2015) 127–134. doi:10.1016/j.jnucmat.2015.01.027.

[18] P.D. Edmondson, C.M. Parish, R.K. Nanstad, Using complimentary microscopy methods to examine Ni-Mn-Si-precipitates in highly-irradiated reactor pressure vessel steels, Acta Mater. 134 (2017) 31–39. doi:10.1016/j.actamat.2017.05.043.

[19] D.J. Sprouster, J. Sinsheimer, E. Dooryhee, S.K. Ghose, P. Wells, T. Stan, N. Almirall, G.R. Odette, L.E. Ecker, Structural characterization of nanoscale intermetallic precipitates in highly neutron irradiated reactor pressure vessel steels, Scr. Mater. 113 (2016) 18–22. doi:10.1016/j.scriptamat.2015.10.019.

[20] T.G. Lach, A. Devaraj, K.J. Leonard, T.S. Byun, Co-dependent microstructural evolution pathways in metastable δ-ferrite in cast austenitic stainless steels during thermal aging, J. Nucl. Mater. 510 (2018) 382–395. doi:10.1016/j.jnucmat.2018.08.038.

[21] H. Ke, P. Wells, P.D. Edmondson, N. Almirall, L. Barnard, G.R. Odette, D. Morgan, Thermodynamic and kinetic modeling of Mn-Ni-Si precipitates in low-Cu reactor pressure vessel steels, Acta Mater. 138 (2017) 10–26. doi:10.1016/j.actamat.2017.07.021.

[22] Y. Matsukawa, T. Takeuchi, Y. Kakubo, T. Suzudo, H. Watanabe, H. Abe, T. Toyama, Y. Nagai, The two-step nucleation of G-phase in ferrite, Acta Mater. 116 (2016) 104–113. doi:10.1016/j.actamat.2016.06.013.

[23] J.-H. Ke, H. Ke, G.R. Odette, D. Morgan, Cluster dynamics modeling of Mn-Ni-Si precipitates in ferritic-martensitic steel under irradiation, J. Nucl. Mater. 498 (2018) 83–88. doi:10.1016/j.jnucmat.2017.10.008.

[24] A. Mateo, L. Llanes, M. Anglada, A. Redjaimia, G. Metauer, Characterization of the intermetallic G-phase in an AISI 329 duplex stainless steel, J. Mater. Sci. 32 (1997) 4533–4540. doi:10.1023/A:1018669217124.

[25] H.J. Beattie, F.L. Versnyder, A New Complex Phase in a High-Temperature Alloy, Nature. 178 (1956) 208–209. doi:10.1038/178208b0.

[26] F.X. Spiegel, D. Bardos, P.A. Beck, Ternary G and E Silicides and Germanides of Transition Elements, Trans. Metall. Soc. AIME. 227 (1963) 575–579.

[27] J.M. Vitek, G-phase formation in aged type 308 stainless steel, Metall. Trans. A. 18 (1987) 154–156. doi:10.1007/BF02646233.

[28] M.K. Miller, J. Bentley, APFIM and AEM investigation of CF8 and CF8M primary coolant pipe steels, Mater. Sci. Technol. 6 (1990) 285–292. doi:10.1179/mst.1990.6.3.285.

[29] X. Yan, A. Grytsiv, P. Rogl, V. Pomjakushin, X. Xue, On the crystal structure of the Mn–Ni–Si G-phase, J. Alloys Compd. 469 (2009) 152–155. doi:10.1016/j.jallcom.2008.01.142.

[30] B. Hu, H. Xu, S. Liu, Y. Du, C. He, C. Sha, D. Zhao, Y. Peng, Experimental investigation and thermodynamic modeling of the Mn–Ni–Si system, Calphad. 35 (2011) 346–354.

[31] I. Shuro, H.H. Kuo, T. Sasaki, K. Hono, Y. Todaka, M. Umemoto, G-phase precipitation in austenitic stainless steel deformed by high pressure torsion, Mater. Sci. Eng. A. 552 (2012) 194–198. doi:10.1016/j.msea.2012.05.030.

[32] S. Li, Y. Wang, X. Wang, F. Xue, G-phase precipitation in duplex stainless steels after long-term thermal aging: A high-resolution transmission electron microscopy study, J. Nucl. Mater. 452 (2014) 382–388. doi:10.1016/j.jnucmat.2014.05.069.

[33] S.L. Li, H.L. Zhang, Y.L. Wang, S.X. Li, K. Zheng, F. Xue, X.T. Wang, Annealing induced recovery of long-term thermal aging embrittlement in a duplex stainless steel, Mater. Sci. Eng. A. 564 (2013) 85–91. doi:10.1016/j.msea.2012.11.046.

[34] W. Guo, D.A. Garfinkel, J.D. Tucker, D. Haley, G.A. Young, J.D. Poplawsky, An atom probe perspective on phase separation and precipitation in duplex stainless steels, Nanotechnology. 27 (2016) 254004. doi:10.1088/0957-4484/27/25/254004.

[35] J.M. Vitek, S.A. David, D.J. Alexander, J.R. Keiser, R.K. Nanstad, Low temperature aging behavior of type 308 stainless steel weld metal, Acta Metall. Mater. 39 (1991) 503–516. doi:10.1016/0956-7151(91)90118-K.

[36] J.W. Cahn, J.E. Hilliard, Free Energy of a Nonuniform System. I. Interfacial Free Energy, J. Chem. Phys. 28 (1958) 258–267. doi:10.1063/1.1744102.

[37] J.W. Cahn, Free Energy of a Nonuniform System. II. Thermodynamic Basis, J. Chem. Phys. 30 (1959) 1121–1124. doi:10.1063/1.1730145.

[38] J.W. Cahn, J.E. Hilliard, Free Energy of a Nonuniform System. III. Nucleation in a Two-Component Incompressible Fluid, J. Chem. Phys. 31 (1959) 688–699. doi:doi:10.1063/1.1730447.

[39] C. Pareige, J. Emo, S. Saillet, C. Domain, P. Pareige, Kinetics of G-phase precipitation and spinodal decomposition in very long aged ferrite of a Mo-free duplex stainless steel, J. Nucl. Mater. 465 (2015) 383–389. doi:10.1016/j.jnucmat.2015.06.017.

[40] R. Badyka, C. Pareige, S. Saillet, C. Domain, Influence of Ni, Mo and Mn Content on the G-Phase Precipitation and Spinodal Decomposition of Aged Duplex Stainless Steels., Microsc. Microanal. 23 (2017) 728–729. doi:10.1017/S1431927617004305.

[41] T.S. Byun, Y. Yang, N.R. Overman, J.T. Busby, Thermal Aging Phenomena in Cast Duplex Stainless Steels, JOM. 68 (2016) 507–516. doi:10.1007/s11837-015-1709-9.

[42] S.V. Rogozhkin, O.A. Korchuganova, A.A. Aleev, Kinetics of α′-phase nucleation during thermal aging of Fe–22% Cr alloy, Inorg. Mater. Appl. Res. 7 (2016) 210–213. doi:10.1134/S2075113316020179.

[43] Z. Yan, Y. Li, X. Zhou, Y. Zhang, R. Hu, Evolution of nanoscale Cr-rich phase in a Fe-35 at.% Cr alloy during isothermal aging, J. Alloys Compd. 725 (2017) 1035–1043. doi:10.1016/j.jallcom.2017.07.221.

[44] Y. Li, Z. Yan, X. Zhou, Kinetics of initial phase separation and coarsening of nanoscale phase in Fe–Cr alloys, J. Nucl. Mater. 497 (2017) 154–160. doi:10.1016/j.jnucmat.2017.07.063.

[45] T. Barkar, L. Höglund, J. Odqvist, J. Ågren, Effect of concentration dependent gradient energy coefficient on spinodal decomposition in the Fe-Cr system, Comput. Mater. Sci. 143 (2018) 446–453. doi:10.1016/j.commatsci.2017.11.043.

[46] A.V. Ponomareva, A.V. Ruban, B.O. Mukhamedov, I.A. Abrikosov, Effect of multicomponent alloying with Ni, Mn and Mo on phase stability of bcc Fe-Cr alloys, Acta Mater. 150 (2018) 117–129. doi:10.1016/j.actamat.2018.02.007.

[47] S. Li, Y. Wang, X. Wang, Effects of Ni content on the microstructures, mechanical properties and thermal aging embrittlement behaviors of Fe–20Cr–xNi alloys, Mater. Sci. Eng. A. 639 (2015) 640–646. doi:10.1016/j.msea.2015.05.063.

[48] J.E. Westraadt, E.J. Olivier, J.H. Neethling, P. Hedström, J. Odqvist, X. Xu, A. Steuwer, A high-resolution analytical scanning transmission electron microscopy study of the early

stages of spinodal decomposition in binary Fe–Cr, Mater. Charact. 109 (2015) 216–221. doi:10.1016/j.matchar.2015.10.001.

[49] J. Zhou, J. Odqvist, L. Höglund, M. Thuvander, T. Barkar, P. Hedström, Initial clustering – a key factor for phase separation kinetics in Fe–Cr-based alloys, Scr. Mater. 75 (2014) 62–65. doi:10.1016/j.scriptamat.2013.11.020.

[50] R. Silva, L.F.S. Baroni, M.B.R. Silva, C.R.M. Afonso, S.E. Kuri, C.A.D. Rovere, Effect of thermal aging at 475°C on the properties of lean duplex stainless steel 2101, Mater. Charact. 114 (2016) 211–217. doi:10.1016/j.matchar.2016.03.002.

[51] J.S. Langer, M. Bar-on, H.D. Miller, New computational method in the theory of spinodal decomposition, Phys. Rev. A. 11 (1975) 1417–1429. doi:10.1103/PhysRevA.11.1417.

[52] J. Emo, C. Pareige, S. Saillet, C. Domain, P. Pareige, Kinetics of secondary phase precipitation during spinodal decomposition in duplex stainless steels: A kinetic Monte Carlo model – Comparison with atom probe tomography experiments, J. Nucl. Mater. 451 (2014) 361–365. doi:10.1016/j.jnucmat.2014.04.025.

[53] P.A. Flinn, Monte Carlo calculation of phase separation in a two-dimensional Ising system, J. Stat. Phys. 10 (1974) 89–97. doi:10.1007/BF01011718.

[54] P. Fratzl, O. Penrose, Kinetics of spinodal decomposition in the Ising model with vacancy diffusion, Phys. Rev. B. 50 (1994) 3477–3480. doi:10.1103/PhysRevB.50.3477.

[55] D.A. Huse, Corrections to late-stage behavior in spinodal decomposition: Lifshitz-Slyozov scaling and Monte Carlo simulations, Phys. Rev. B. 34 (1986) 7845–7850. doi:10.1103/PhysRevB.34.7845.

[56] G.S. Grest, D.J. Srolovitz, Structure and evolution of quenched Ising clusters, Phys. Rev. B. 30 (1984) 5150–5155. doi:10.1103/PhysRevB.30.5150.

[57] J.L. Lebowitz, J. Marro, M.H. Kalos, Dynamical scaling of structure function in quenched binary alloys, Acta Metall. 30 (1982) 297–310. doi:10.1016/0001-6160(82)90069-4.

[58] G.F. Mazenko, O.T. Valls, Model Theory for Spinodal Decomposition, Phys. Rev. Lett. 51 (1983) 2044–2047. doi:10.1103/PhysRevLett.51.2044.

[59] A. Milchev, D.W. Heermann, K. Binder, Monte-Carlo simulation of the Cahn-Hillard model of spinodal decomposition, Acta Metall. 36 (1988) 377–383. doi:10.1016/0001-6160(88)90013-2.

[60] C. Pareige, M. Roussel, S. Novy, V. Kuksenko, P. Olsson, C. Domain, P. Pareige, Kinetic study of phase transformation in a highly concentrated Fe–Cr alloy: Monte Carlo simulation versus experiments, Acta Mater. 59 (2011) 2404–2411.

[61] M. Rao, M.H. Kalos, J.L. Lebowitz, J. Marro, Time evolution of a quenched binary alloy. III. Computer simulation of a two-dimensional model system, Phys. Rev. B. 13 (1976) 4328–4335. doi:10.1103/PhysRevB.13.4328.

[62] C. Roland, M. Grant, Monte Carlo Renormalization-Group Study of the Late-Stage Dynamics of Spinodal Decomposition, Phys. Rev. Lett. 60 (1988) 2657–2660. doi:10.1103/PhysRevLett.60.2657.

[63] J.M. Hyde, M.K. Miller, M.G. Hetherington, A. Cerezo, G.D.W. Smith, C.M. Elliott, Spinodal decomposition in Fe-Cr alloys: Experimental study at the atomic level and comparison with computer models—II. Development of domain size and composition amplitude, Acta Metall. Mater. 43 (1995) 3403–3413. doi:10.1016/0956-7151(95)00041-S.

[64] J.M. Hyde, A. Cerezo, M.K. Miller, G.D.W. Smith, A critical comparison between experimental results and numerical simulations of phase separation in the Fe-Cr system, Appl. Surf. Sci. 76–77 (1994) 233–241. doi:10.1016/0169-4332(94)90348-4.

[65] C. Pareige, S. Novy, S. Saillet, P. Pareige, Study of phase transformation and mechanical properties evolution of duplex stainless steels after long term thermal ageing (>20 years), J. Nucl. Mater. 411 (2011) 90–96. doi:10.1016/j.jnucmat.2011.01.036.

[66] F. Danoix, P. Auger, D. Blavette, Hardening of Aged Duplex Stainless Steels by Spinodal Decomposition, Microsc. Microanal. 10 (2004) 349–354.

[67] D. Blavette, P. Auger, Fine scale investigation of some phenomena in metallic alloys by field ion microscopy and atom probe microanalysis, Microsc. Microanal. Microstruct. 1 (1990) 481–492. doi:10.1051/mmm:0199000105-6048100.

[68] F. Danoix, P. Auger, D. Blavette, An atom-probe investigation of some correlated phase transformations in Cr, Ni, Mo containing supersaturated ferrites, Surf. Sci. 266 (1992) 364–369. doi:10.1016/0039-6028(92)91047-F.

[69] F. Bley, Neutron small-angle scattering study of unmixing in Fe-Cr alloys, Acta Metall. Mater. 40 (1992) 1505–1517. doi:10.1016/0956-7151(92)90094-U.

[70] M. Furusaka, Y. Ishikawa, S. Yamaguchi, Y. Fujino, Phase Separation Process in FeCr Alloys Studied by Neutron Small Angle Scattering, J. Phys. Soc. Jpn. 55 (1986) 2253–2269. doi:10.1143/JPSJ.55.2253.

[71] J.C. LaSalle, L.H. Schwartz, Further studies of spinodal decomposition in Fe-Cr, Acta Metall. 34 (1986) 989–1000. doi:10.1016/0001-6160(86)90208-7.

[72] T. Ujihara, K. Osamura, Kinetic analysis of spinodal decomposition process in Fe–Cr alloys by small angle neutron scattering, Acta Mater. 48 (2000) 1629–1637. doi:10.1016/S1359-6454(99)00441-3.

[73] D. Blavette, G. Grancher, A. Bostel, Statistical Analysis of Atom-Probe Data (I) : Derivation of some Fine-Scale Features from Frequency Distributions for Finely Dispersed Systems, J. Phys. Colloq. 49 (1988) 433–438. doi:10.1051/jphyscol:1988674.

[74] J. Zhou, J. Odqvist, M. Thuvander, P. Hedström, Quantitative Evaluation of Spinodal Decomposition in Fe-Cr by Atom Probe Tomography and Radial Distribution Function Analysis, Microsc. Microanal. 19 (2013) 665–675. doi:10.1017/S1431927613000470.

[75] G. Bandel, W. Tofaute, Die Versprödung von hochlegierten Chromstählen im Temperaturgebiet um 500°., Arch. Für Eisenhüttenwes. 15 (1942) 307–320.

[76] P. Hedström, F. Huyan, J. Zhou, S. Wessman, M. Thuvander, J. Odqvist, The 475°C embrittlement in Fe–20Cr and Fe–20Cr–X (X=Ni, Cu, Mn) alloys studied by mechanical testing and atom probe tomography, Mater. Sci. Eng. A. 574 (2013) 123–129. doi:10.1016/j.msea.2013.03.016.

[77] M.K. Miller, J.M. Hyde, A. Cerezo, G.D.W. Smith, Comparison of low temperature decomposition in Fe-Cr and duplex stainless steels, Appl. Surf. Sci. 87–88 (1995) 323–328. doi:10.1016/0169-4332(95)00497-1.

[78] B. Gault, M.P. Moody, J.M. Cairney, S.P. Ringer, Specimen Preparation, in: At. Probe Microsc., Springer, Springer, 2012: pp. 71–110.

[79] F. Zhang, J. Ilavsky, G.G. Long, J.P.G. Quintana, A.J. Allen, P.R. Jemian, Glassy Carbon as an Absolute Intensity Calibration Standard for Small-Angle Scattering, Metall. Mater. Trans. A. 41 (2010) 1151–1158. doi:10.1007/s11661-009-9950-x.

[80] M. Hennion, I. Mirebeau, Diffusion de neutrons aux petits angles (DNPA) et magnétisme: concepts et applications, J. Phys. IV. 09 (1999) Pr1-51. doi:10.1051/jp4:1999104.

[81] E. Rauch, A. Duft, Orientation maps derived from TEM diffraction patterns collected with an external CCD camera, Mater. Sci. Forum. 495–497 (2005) 197–202.

[82] E.F. Rauch, M. Véron, Automated crystal orientation and phase mapping in TEM, Mater. Charact. 98 (2014) 1–9. doi:10.1016/j.matchar.2014.08.010.

[83] L. Couturier, F. De Geuser, M. Descoins, A. Deschamps, Evolution of the microstructure of a 15-5PH martensitic stainless steel during precipitation hardening heat treatment, Mater. Des. 107 (2016) 416–425. doi:10.1016/j.matdes.2016.06.068.

[84] Y.R. Wen, Y.P. Li, A. Hirata, Y. Zhang, T. Fujita, T. Furuhara, C.T. Liu, A. Chiba, M.W. Chen, Synergistic alloying effect on microstructural evolution and mechanical properties of Cu precipitation-strengthened ferritic alloys, Acta Mater. 61 (2013) 7726–7740. doi:10.1016/j.actamat.2013.09.011.

[85] Z.B. Jiao, J.H. Luan, Z.W. Zhang, M.K. Miller, W.B. Ma, C.T. Liu, Synergistic effects of Cu and Ni on nanoscale precipitation and mechanical properties of high-strength steels, Acta Mater. 61 (2013) 5996–6005. doi:10.1016/j.actamat.2013.06.040.

[86] S. Shu, B.D. Wirth, P.B. Wells, D.D. Morgan, G.R. Odette, Multi-technique characterization of the precipitates in thermally aged and neutron irradiated Fe-Cu and Fe-Cu-Mn model alloys: Atom probe tomography reconstruction implications, Acta Mater. 146 (2018) 237–252. doi:10.1016/j.actamat.2017.12.006.

[87] F. DeGeuser, W. Lefebvre, Determination of matrix composition based on solute-solute nearest-neighbor distances in atom probe tomography, Microsc. Res. Tech. 74 (2011) 257–263. doi:10.1002/jemt.20899.

[88] V.F. Sears, Thermal-neutron scattering lengths and cross sections for condensed-matter research, Chalk River Nuclear Laboratories, Chalk River, Ontario, 1984.

[89] M.H. Mathon, A. Barbu, F. Dunstetter, F. Maury, N. Lorenzelli, C.H. de Novion, Experimental study and modelling of copper precipitation under electron irradiation in dilute FeCu binary alloys, J. Nucl. Mater. 245 (1997) 224–237. doi:10.1016/S0022-3115(97)00010-X.

[90] A. Deschamps, F. DeGeuser, On the validity of simple precipitate size measurements by small-angle scattering in metallic systems, J. Appl. Crystallogr. 44 (2011) 343–352. doi:10.1107/S0021889811003049.

[91] F. De Geuser, A. Deschamps, Precipitate characterisation in metallic systems by small-angle X-ray or neutron scattering, Comptes Rendus Phys. 13 (2012) 246–256. doi:10.1016/j.crhy.2011.12.008.

[92] P. Chaudouet, R. Madar, R. Fruchart, B. Lambert, Etude de nouveaux pnictures ternaires de metaux de transition isostructuraux des phases G, Ni16Mn6P7, Ni16Mn6As7, Mater. Res. Bull. 18 (1983) 713–719. doi:10.1016/0025-5408(83)90098-3.

[93] K.H. Lo, C.H. Shek, J.K.L. Lai, Recent developments in stainless steels, Mater. Sci. Eng. R Rep. 65 (2009) 39–104. doi:10.1016/j.mser.2009.03.001.

[94] A.T. Aldred, Ferromagnetism in iron-chromium alloys. I. Bulk magnetization measurements, Phys. Rev. B. 14 (1976) 219–227. doi:10.1103/PhysRevB.14.219.

[95] L. Couturier, F. De Geuser, A. Deschamps, Direct comparison of Fe-Cr unmixing characterization by atom probe tomography and small angle scattering, Mater. Charact. 121 (2016) 61–67. doi:10.1016/j.matchar.2016.09.028.

[96] D. Isheim, M.S. Gagliano, M.E. Fine, D.N. Seidman, Interfacial segregation at Cu-rich precipitates in a high-strength low-carbon steel studied on a sub-nanometer scale, Acta Mater. 54 (2006) 841–849. doi:10.1016/j.actamat.2005.10.023.

[97] B. Gault, M.P. Moody, J.M. Cairney, S.P. Ringer, Atom Probe Microscopy, Springer, Springer, 2012.

[98] F. Vurpillot, B. Gault, B.P. Geiser, D.J. Larson, Reconstructing atom probe data: A review, Ultramicroscopy. 132 (2013) 19–30. doi:10.1016/j.ultramic.2013.03.010.

[99] P. Auger, F. Danoix, A. Menand, S. Bonnet, J. Bourgoin, M. Guttmann, Atom probe and transmission electron microscopy study of aging of cast duplex stainless steels, Mater. Sci. Technol. 6 (1990) 301–313. doi:10.1179/mst.1990.6.3.301.

[100] A.W. Bowen, G.M. Leak, Diffusion in Bcc iron base alloys, Metall. Trans. 1 (1970) 2767–2773. doi:10.1007/BF03037813.

[101] R.A. Wolfe, H.W. Paxton, Diffusion in b.c.c. metals, Carnegie Inst of Tech, Pittsburgh, PA, 1964. https://apps.dtic.mil/docs/citations/AD0434751 (accessed July 30, 2019).

[102] A.-M. Huntz, M. Aucouturier, P. Lacombe, Mesure des coefficients de diffusion en volume et intergranulaire du chrome radioactif dans le fer alpha, Comptes Rendus Académie Sci. 265 (1967) 554–557.

[103] F. Danoix, P. Auger, Atom Probe Studies of the Fe–Cr System and Stainless Steels Aged at Intermediate Temperature: A Review, Mater. Charact. 44 (2000) 177–201. doi:10.1016/S1044-5803(99)00048-0.

[104] J.E. Brown, G.D.W. Smith, Atom probe studies of spinodal processes in duplex stainless steels and single- and dual-phase Fe-Cr-Ni alloys, Surf. Sci. 246 (1991) 285–291. doi:10.1016/0039-6028(91)90428-U.

[105] T.R. Leax, S.S. Brenner, J.A. Spitznagel, Atom probe examination of thermally ages CF8M cast stainless steel, Metall. Trans. A. 23 (1992) 2725–2736. doi:10.1007/BF02651752.

[106] J.M. Hyde, M.K. Miller, A. Cerezo, G.D.W. Smith, A study of the effect of ageing temperature on phase separation in Fe-45%Cr alloys, Appl. Surf. Sci. 87–88 (1995) 311–317.

[107] M. Kato, Hardening by spinodally modulated structure in b.c.c. alloys, Acta Metall. 29 (1981) 79–87. doi:10.1016/0001-6160(81)90088-2.

Supplementary material

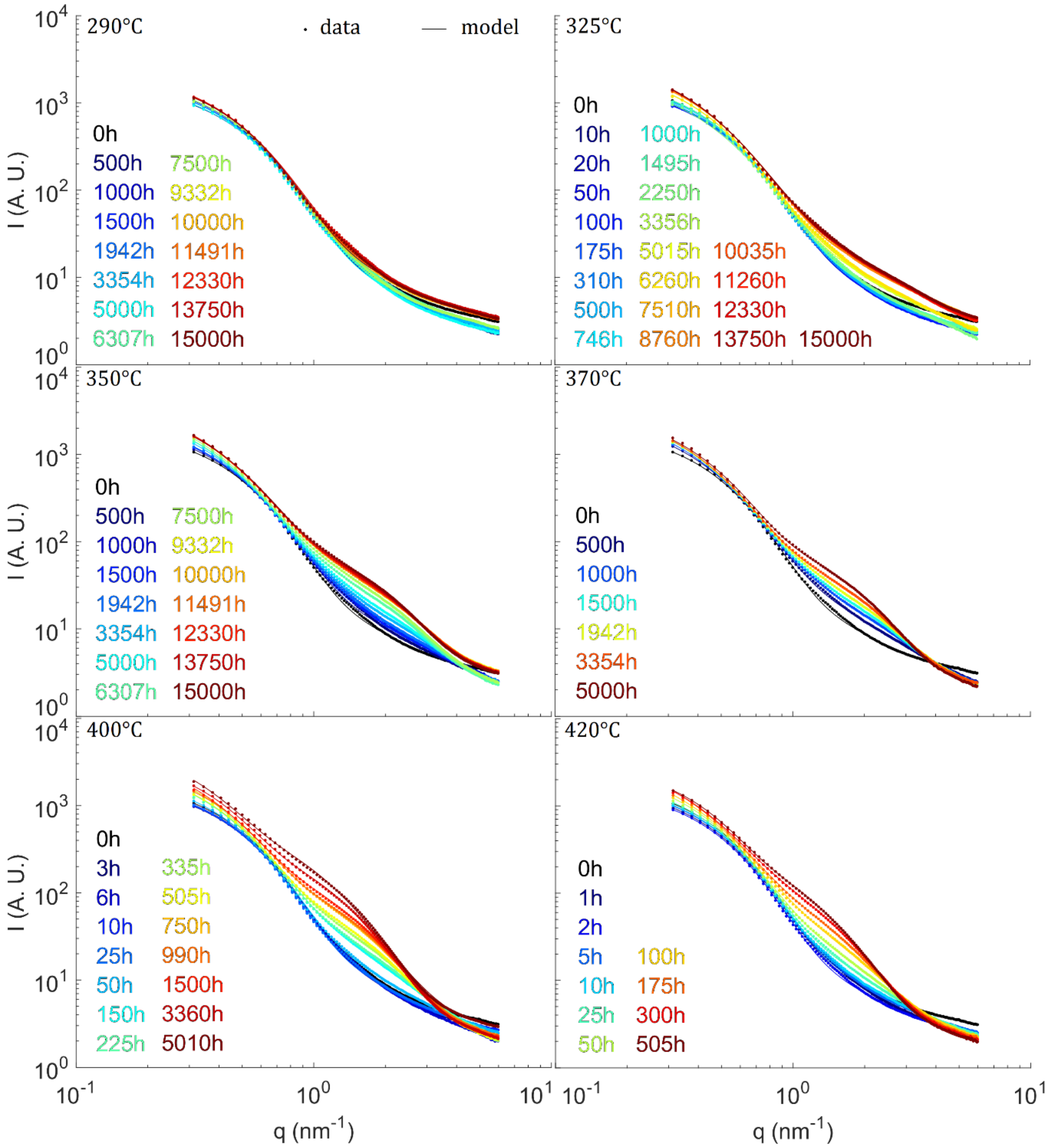

Figure 13 : All SAXS data for the six different aging temperatures together with their corresponding model. The color scale goes from dark blue for the smallest aging duration to dark red for the longest, unaged condition is displayed in black (0h).

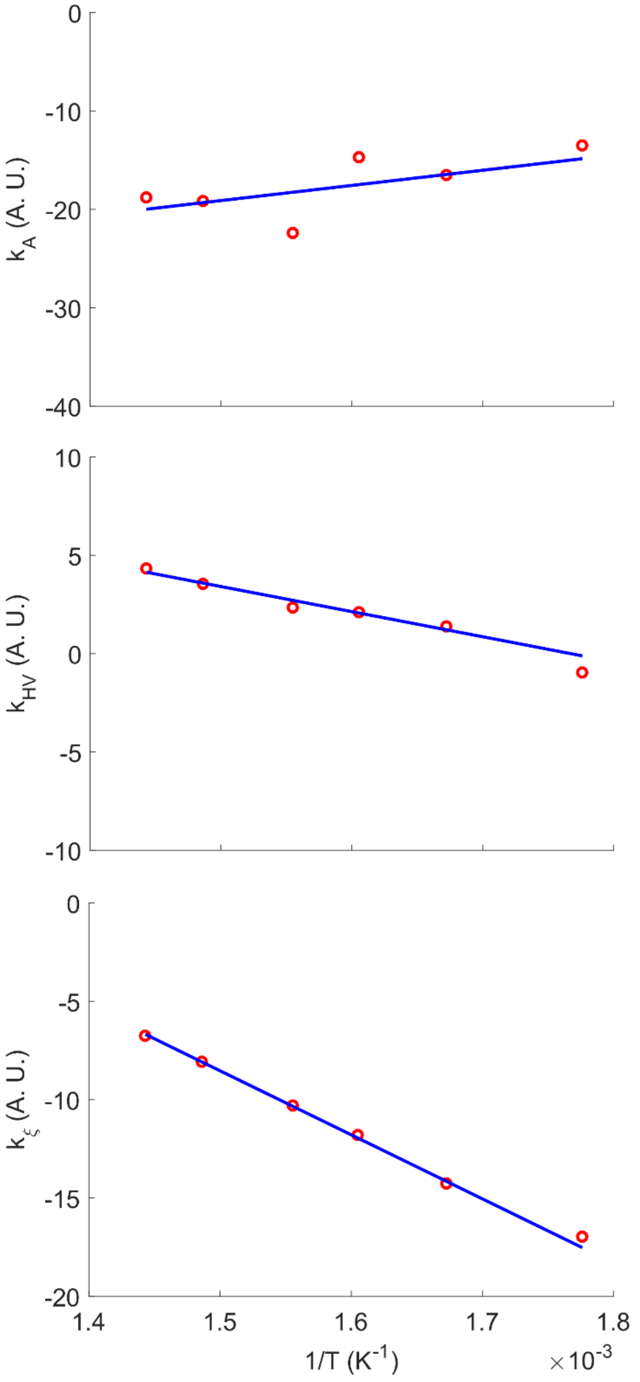

Figure 14 : Arrhenius plots of the power laws pre-factors describing the evolutions of the amplitude (top graph), the hardness increment (middle graph) and the coherency length (bottom graph).

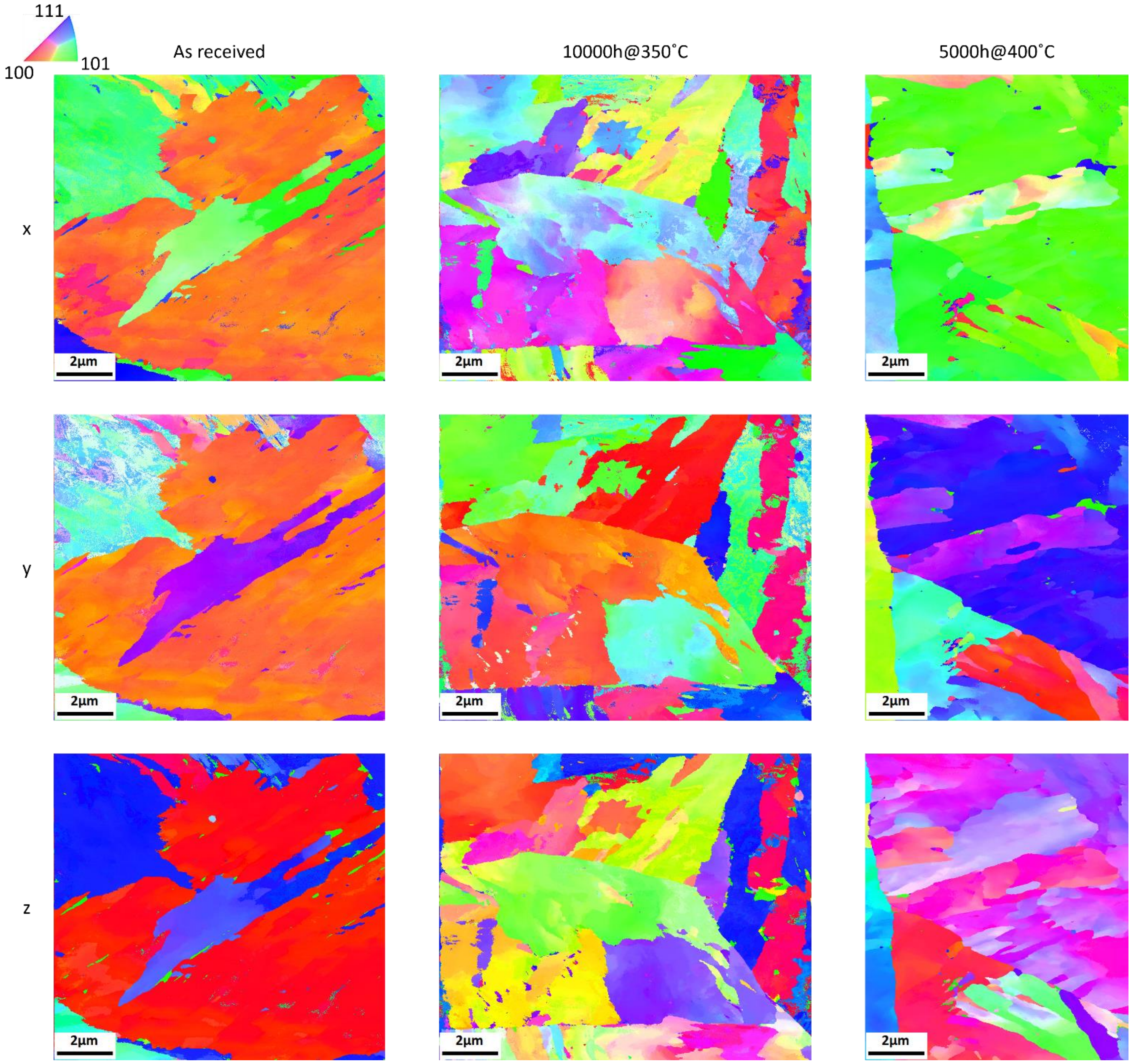

Figure 15: Crystallographic orientations maps in three perpendicular directions x, y and z corresponding to the phases maps presented in Figure 1 (three conditions: as received on the left hand-side, 10000h@350°C in the middle and 5000h@400°C on the right hand-side). Each color corresponds to a crystallographic orientation according to the orientation triangle displayed on top left hand-side of this figure.